Visualisation method for the broad distribution of seafloor ferromanganese deposits

Machida, Shiki ; Sato, Taichi ; Yasukawa, Kazutaka ; Nakamura, Kentaro ; Iijima, Koichi ; Nozaki, Tatsuo ; Kato, Yasuhiro
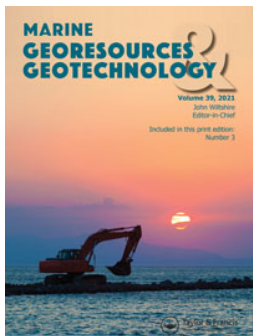
Visualisation method for the broad distribution of seafloor ferromanganese deposits

Shiki Machida, Taichi Sato, Kazutaka Yasukawa, Kentaro Nakamura, Koichi Iijima, Tatsuo Nozaki & Yasuhiro Kato

View supplementary material ⧉

Published online: 03 Dec 2019.

Submit your article to this journal ⧉

Article views: 1008

View related articles ⧉

View Crossmark data ⧉

Citing articles: 2 View citing articles ⧉

Taylor & Francis
Taylor & Francis Group

🔓 OPEN ACCESS | Check for updates

Visualisation method for the broad distribution of seafloor ferromanganese deposits

Shiki Machida[a,b], Taichi Sato[c], Kazutaka Yasukawa[a,b,d], Kentaro Nakamura[d], Koichi Iijima[e], Tatsuo Nozaki[a,b,e,f] and Yasuhiro Kato[a,b,d,e]

[a]Ocean Resources Research Center for Next Generation (ORCeNG), Chiba Institute of Technology, Narashino, Japan; [b]Frontier Research Center for Energy and Resources (FRCER), School of Engineering, The University of Tokyo, Tokyo, Japan; [c]Geological Survey of Japan, National Institute of Advanced Industrial Science and Technology (AIST), Tsukuba, Japan; [d]Department of Systems Innovation, School of Engineering, The University of Tokyo, Tokyo, Japan; [e]Submarine Resources Research Center, Research Institute for Marine Resources Utilization, Japan Agency for Marine-Earth Science and Technology (JAMSTEC), Yokosuka, Japan; [f]Department of Planetology, Graduate School of Science, Kobe University, Kobe, Japan

ABSTRACT

The increasing global demand for industrially critical metals has driven the development of deep-sea mineral resources. In the past, acoustic exploration has been utilised as an efficient technique for investigating deep-sea mineral resources. However, a practical method applicable to a wide distribution of resources has not yet been established. We show that the acoustic backscatter intensity of the seafloor determined using a vessel-equipped multi-narrow beam echo sounder provides an inherent threshold that bounds different types of geology, e.g. barren pelagic sediment and dense ferromanganese nodules. We found that multiple datasets from different sounders and/or the observation periods could be integrated on the basis of the thresholds that indicate the same geological boundaries. Furthermore, the integrated data and threshold provided visualisation and quantitative estimations regarding the distribution of ferromanganese deposits covering thousands of square kilometres. Our method is applicable after minimal data processing and ground-truth observations, and provides expeditious and exhaustive reconnaissance exploration.

1. Introduction

The interest in deep-sea minerals (Hannington et al. 2011; Hein et al. 2013; Kato et al. 2011) has considerably increased because these minerals include critical metals (e.g. Co, Ni, Au, Ag, Mo, Te, W, Pt, Bi, Sc, Y, and rare-earth elements), which are in demand for applications in highly advanced, green energy technologies that could be used by future generations. The first step in mining and utilising deep-sea minerals, particularly ferromanganese deposits (nodules and/or crusts), is the development of an efficient method that can explore vast areas during reconnaissance exploration to find unknown distribution of the resources and narrow down the high potential region(s). A large number of primary explorations since the 1970s that used a freefall grab, box corer, deep-tow photography system or submersible dive (or a combination of these approaches) revealed that the distribution density of ferromanganese nodules fluctuates over various spatial scales in response to a changing topography and the thickness of the associated pelagic sediment (Cochonat et al. 1992; Craig 1979; Piper and Blueford 1982; Sharma and Kodagali 1993; Sharma, Khadge, and Jai Sankar

2013; Usui et al. 1987; Valsangkar and Rebello 2015). However, a critical problem in using such equipment (except for submersible observation) is the requirement of extensive effort when analysing vast areas, owing to a low spatial resolution and requirement of quite large number of data points (sampling points). For highly effective exploration in terms of cost and time, a method to focus on target areas from a broad and evenly explored area is required.

To efficiently investigate a broad area, exploration using sound waves is valid. In particular, the exploration using a multi-narrow beam echo sounder (MBES) has demonstrated high potential in searching for hydrothermal activities since practical methods (Chadwick et al. 2014; Kasaya et al. 2015; Nakamura et al. 2015; Roman et al. 2012) have been proposed. However, these methods rely on detecting a unique hydrothermal phenomenon as a water column anomaly, i.e. the belching of plumes and/or CO_2 bubbles from hydrothermal vents. Even though these methods are useful for observing the presence of hydrothermal activity and/or gas emissions, but do not constrain the spread of ore bodies and mineral deposits, because detected signals are not from seafloor. Therefore, these methods cannot be generally applied.

Acoustic backscattering of the seafloor is thought to provide a useful signal representing the existence of ferromanganese nodules on the seafloor (de Moustier 1986). Basic (de Moustier and Matsumoto 1993) and theoretical (Ma et al. 1986; de Moustier 1985; Tolstoy 1983) studies in the early stage of nodule exploration constrained this concept for processing MBES backscatter data. Indeed, certain applications using a deep-towed side scan sonar (Lee and Kim 2004; Wiedicke and Weber 1996) demonstrate high-resolution mapping results for nodule fields at once only covering an area of several hundreds of square metres. In contrast, some previous investigations using vessel-equipped MBES identified variations of distributions over an area of tens or hundreds of square kilometres of lava (Hirano et al. 2006, 2008, 2013, 2016) or nodules (Chakraborty and Kodagali 2004; Chunhui et al. 2015; Machida et al. 2016) based on backscatter intensity levels. Therefore, vessel-equipped MBES can provide a more economical exploration for vast areas than that provided by underwater apparatuses. However, a disadvantage inhibiting its use is that the different physical and technical parameters, such as sounder characteristics, observation period and processing, yield different absolute values of backscatter intensity for the same area. As a solution, we propose a simple method for reconnaissance exploration to obtain a widespread distribution of deep-sea ferromanganese nodules, using a combination of several datasets of vessel-equipped MBES.

2. Materials and methods

2.1. Field observations

The Japanese exclusively economic zone (EEZ) around Minamitorishima Island in the western North Pacific (Figure 1) is the best candidate area in which to analyse vessel-equipped multibeam backscatter data. This is due to the fact that several research cruises, operated by the Japan Agency for Marine-Earth Science and Technology (JAMSTEC), have obtained multiple sets of backscatter data, combined with bathymetry mapping (Figure S1, supplementary material). These data were obtained with an identical MBES for each of the four cruises of R/V Mirai (MR14-E02, MR15-E01 Legs 2 and 3 and MR15-02) in 2014 and 2015 (Figures S2–S5, supplementary material). We also reprocessed previous cruise data (Machida et al. 2016), which were obtained during a cruise YK10-05 of R/V Yokosuka in 2010, to verify analytical reproducibility for the different MBESs and cruise periods. Data coverage is mainly in the central and eastern region of the Japanese EEZ around Minamitorishima Island (Figure S6, supplementary material). To provide ground-truthing of the measured backscatter intensities, we performed 13 dives of the submersible SHINKAI 6500 (Figures S2–S6, supplementary material) during two cruises of R/V Yokosuka (YK16-01 and YK17-11C, in 2016 and 2017, respectively) in the target region. Various distribution features for ferromanganese nodules on pelagic sediment (Table S1 and Figures S7–S28, supplementary material) were observed at all dive sites. We determined the nodule distribution density by using the blue/yellow-banded box with a side of 50 cm. For dives along a
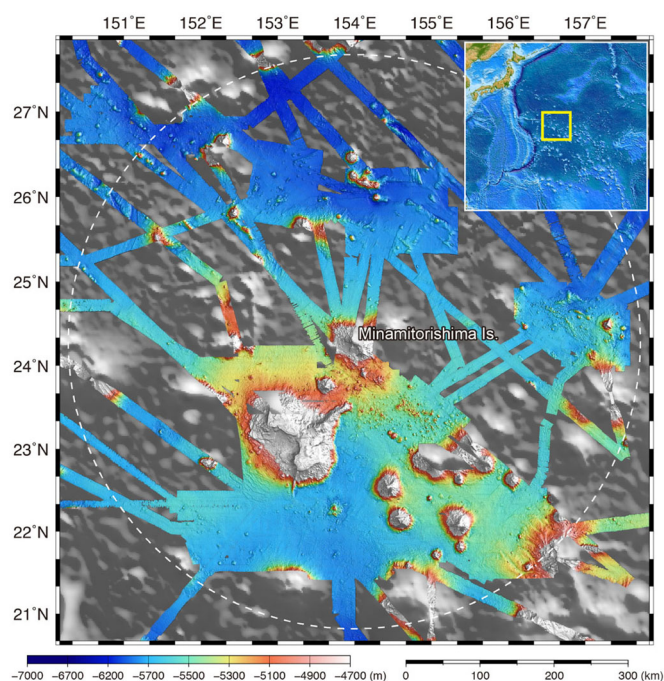

Figure 1. Topography for the Japanese exclusive economic zone (EEZ) around Minamitorishima Island. Range for the main map is indicated by a yellow box in the index map in the upper right-hand corner. Coloured topographic data in the main map were determined using a vessel-equipped multi-narrow beam echo sounder (MBES) developed by the Japan Agency for Marine-Earth Science and Technology (JAMSTEC). Details of the data and cruises presented in this study are described in the materials and methods section and in Supporting Figures. Topographic data for the grey background of the main map and the map in the upper right-hand corner are from ETOPO1 (NOAA National Geophysical Data Center). The white dashed line shows the Japanese EEZ around Minamitorishima Island.

slope of seamount or guyot (6 K#1463, 6 K#1497 and 6 K#1499; Figures S14, S16, S21, S22, S25 and S26, supplementary material), we observed continuous distributions of ferromanganese nodule fields and outcrops covered by ferromanganese crust. We also observed intrusions or flows of lava (volcanic rock) covered by thin ferromanganese crusts which were also observed at site 6 K#1466 (Figures S19 and S20, supplementary material).

R/V Mirai and R/V Yokosuka were equipped with a SeaBeam 3012. multibeam system composed of 301 beams with an operating frequency of 12 kHz and a SeaBeam 2112.004 multibeam system composed of 151 beams with an operating frequency of 12 kHz, respectively. The sound velocity correction used real-time data from the surface water velocity metre and the sound velocity profiles obtained by an expendable Conductivity Temperature Depth profiler (XCTD) and an eXpendable BathyThermograph (XBT) during the cruises in the study area. The software, HIPS and SIPS 10.4 (Teledyne CARIS; Ltd., Fredericton, Canada) was used to remove extreme depth variation in swath data and post-processing backscatter data.

Because acoustic signals can penetrate seafloor sediments, features observed in multibeam backscatter images are considered to be buried beneath the surface. The calculated penetration depth in the case of a frequency of 12 kHz is about 3–20 m, which depends on the grazing angle (Mitchell 1993). In contrast, the depth accuracy of MBES for this survey is about ±30 m, which is similar to the previously

reported values (International Hydrographic Organization 2008; Oikawa et al. 2010). Therefore, we consider that the observed signal directly reflects from the seafloor, which is the most significant boundary of physical properties. However, horizontal resolution ranges 40-120 m. Thus, backscatter intensity should reflect the tendency of the general features on seafloor facies and its changes over a distance of several tens of metres. Hence, we should assume minor inconsistencies between the results of in-situ observation by the SHINKAI 6500 and the processed bathymetry and backscatter intensity data in some cases. However, we consider that spatial resolution is still enough for the objectives of this study, i.e. for the method for regional scale reconnaissance exploration. We note that the thickness of the ferromanganese layers is not constrained by our method, particularly in the ferromanganese crust region.

2.2. Data processing

To correct the backscatter data, beam pattern correction was applied to remove acoustic artefacts caused by angular response in the sonar from the imagery. However, we inferred that beam pattern correction represented by one beam pattern for the data obtained during the same cruise would be insufficient, because our survey area was vast. Therefore, we separated the survey area into two areas (the northern and southern areas of the Japanese EEZ around Minamitorishima Island), and then beam pattern corrections were applied by using each beam pattern for each area. The transit data obtained during each cruise were processed separately. As a result, the backscatter intensity data were divided into seven subsets named MR14-E02south, MR15-E01south, MR15-E01north, MR15-02south, MR14-E02transit MR15-E01transit, and MR15-02transit for data collected by R/V Mirai (Figures S2–S5, supplementary material) and two subsets named YK10-05SiteA and B for data collected by R/V Yokosuka (Figure S6, supplementary material). Beam pattern files were created using the SIPS Side Scan engine. For consistent processed backscatter data, as much data as possible should be used to create the files. After processing for gain normalisation and despeckle noise, the backscatter grid files were produced using the SIPS Side Scan engine. Although the horizontal resolution ranges from 40 to 120 m as previously mentioned, a 50-m grid interval is chosen to create bathymetry and backscatter intensity grids because high-density MBES surveys were conducted in the study area. We used the Generic Mapping Tools (GMT) software (Wessel and Smith 1998) to plot the datasets and produce wide-swath topographic maps and acoustic backscatter images of the seafloor. The straight lines in each backscatter images are artefacts owing to error data commonly observed around and just below the ship track.

3. Results

To analyse the correspondence between geological features and backscatter intensity, we used the region approximately 200 km south of the Minamitorishima Island as a type

location (Figure 2) owing to the following advantages: (i) the existence of multiple sets of data obtained by the same MBES for different periods (MR14-E02south, MR15-E01south and MR15-02south; see the materials and methods section for details) and (ii) the comprehensive coverage of the variance of backscatter intensity and ground-truthing observations using the submersible SHINKAI 6500 (dive Nos. 6 K#1461, #1464 and #1465). Correspondence between the distribution of ferromanganese nodules and backscatter intensity was investigated during dives of the submersible SHINKAI 6500. From snapshots taken to exhibit typical features of nodule distribution (Figure 2), we recognised four types of seafloor facies. Type-L facies correspond with a low backscatter intensity, which is characterised by a sparse distribution of small nodules on a pelagic sediment (stop 1 of Site 6 K#1461 and #1465; Figure S13, supplementary material). Type-M facies correspond with a medium backscatter intensity, which is characterised by a sparse distribution of large flattened nodules (stops 3 and 4 of Site 6 K#1465; Figure S13, supplementary material) or a dense distribution of small equi-granular rounded nodules (stops 3, 5 and 6 of 6 K#1464; Figure S18, supplementary material). Type-H facies correspond with a high backscatter intensity, which is characterised by a dense distribution of rounded nodules showing a bimodal size distribution (stop 4 of Site 6 K#1464; Figure S18, supplementary material). Type-V facies correspond with a very high backscatter intensity, which is characterised by an almost full coverage of rounded nodules showing a bimodal grain size distribution (stops 1 and 2 of Site 6 K#1464; Figure S18, supplementary material).

Regardless of which cruise collected a dataset, each region reproduced identical differences in backscatter intensity with each facies of nodule distribution (Figure 2). Furthermore, we commonly observed correlations between the backscatter intensity and the nodule distribution density (Figures S7–S28, supplementary material) at all dive sites in the entire dataset region, even outside the type location (will be discussed in detail in the following section). These observations are consistent with previous theoretical investigations (Chunhui et al. 2015). An exception to these consistencies was observed at site 6 K#1460 (Figures S10 and S11; Table S1, supplementary material) caused by a cover of thin pelagic sediment on a dense ferromanganese nodule field. In this case, even though seafloor backscatter intensity is strong, the nodule distribution density, based on megascopic observation, appears low.

At the boundary between the two seafloor facies, one facies gradually shifts to another by repeatedly changing to both facies over a distance of several tens of metres. We commonly observed such gradual changes in facies along the SHINKAI 6500 dive track, e.g. from stop 1 to 2 during the 6 K#1501 dive (a snap shot of the boundary between Type-L and Type-M facies is shown in Figure S9, supplementary material). In contrast, we observed a sudden transition from a ferromanganese nodule field to an outcrop covered by ferromanganese crust at regions with Type-H or Type-V facies, e.g. after stop 5 of the 6 K#1463 dive (Figures S14 and S15, supplementary material), from stop 2 to 3
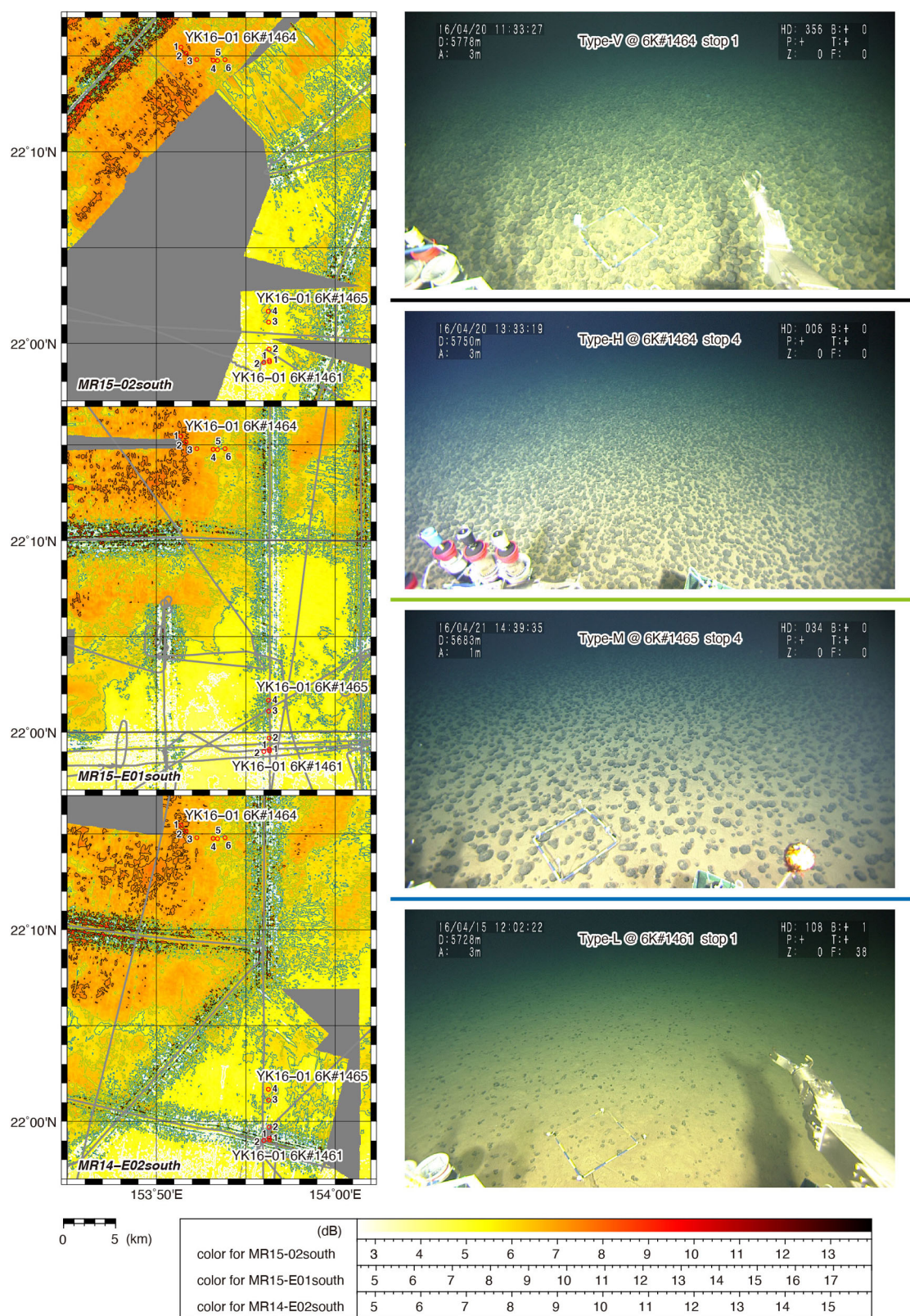
Figure 2. Map of backscatter intensity and ground-truthing observations in the type location approximately 200 km south of Minamitorishima Island. Multiple sets of backscatter intensity data (MR14-E02south, MR15-E01south and MR15-02south) are shown in the different panels on the left. The range of the map for each dataset is the same and is shown as a white box in Figures S2–S4 (supplementary material). Grey lines illustrate ship track of each cruises. Photographs on the right show the types of seafloor facies (Type-L, Type-M, Type-H and Type-V facies; see the main text for details) and are taken at stops (red circles on the map, with numeric annotation indicating stop numbers) during three dives of the submersible *SHINKAI 6500* (dive Nos. 6 K#1461, #1464 and #1465; see supplementary material for details). One side of the blue/yellow-banded box is 50 cm. Geographic distributions of the seafloor showing values of the boundary intensities between the different types of seafloor facies, i.e. L–M, M–H and H–V boundaries (see the main text, Figure 3 and Table 1 for details), are illustrated blue, green and black contour lines, respectively, in the intensity maps. The white contour line indicates the geographic distribution of the seafloor showing the base intensity (see the main text, Figure 3 and Table 1).

Table 1. Specific values for each set of backscatter intensity data.

Data name	Base intensity (dB)	Boundary intensity (dB)			Relative Interval		Conversion factor (κ)
		LM	MH	HV	MH_{RI}	HV_{RI}	
MR14-E02south	6.70	7.65	8.20	9.20	0.63	0.60	0.93
MR14-E02transit	7.50	8.20	8.60	9.30	0.64	0.61	0.67
MR15-E01south	7.00	8.20	8.90	10.20	0.63	0.59	1.19
MR15-E01north	8.05	8.90	9.40	10.30	0.63	0.60	0.83
MR15-E01transit	6.25	7.10	7.60	8.50	0.63	0.60	0.83
MR15-02south	4.75	5.80	6.40	7.45	0.64	0.61	1.00
MR15-02transit	6.50	7.20	7.60	8.30	0.64	0.61	0.67
YK10-05Site A	3.20	9.60	13.20	19.60	0.64	0.61	6.07
YK10-05Site B	4.80	9.20	11.80	16.40	0.63	0.60	4.30
Integrated	4.75	5.72	6.30	7.30	0.63	0.61	

during the 6 K#1497 dive (Figures S21 and S22, supplementary material) and at stop 2 of the 6 K#1499 dive (Figures S25 and S26, supplementary material). Type-L facies include both regions with barren pelagic sediment that lack nodules (6 K#1503; Figures S27 and S28, supplementary material) and regions with a sparse small nodule distribution.

4. Discussion

4.1. Histogram analysis: Basic concept of a simple method for reconnaissance exploration based on vessel-equipped MBES data

We found that histogram of backscatter intensity is useful to quantitatively investigate the correlations between backscatter intensity and seafloor facies, and to compare or integrate multiple sets of MBES data. For the first of all discussion to propose our method for reconnaissance exploration based on vessel-equipped MBES data, we focus on the MR15-02south data which should be used as a reference amongst the three sets of data for the type location (Figure 2), because we did not observe error backscatter intensity data (commonly observed just below the ship track) at any stop during dives of the *SHINKAI 6500* (Figures S12, S13, S17 and S18, supplementary material). A histogram of backscatter intensity for the MR15-02south data in the type location is shown in Figure 3a. Data variance of this region fully covers the entire data variance of the MR15-02south data as mentioned in Section 3. Therefore, data bias should be limited. The histogram shows multiple peaks in the frequency distribution. We thus calculated the first- and second-order differential values of the intensity data. Because intrinsic changes in frequency cannot be recognised merely by the apparent shape of the histogram (e.g. some peaks are almost buried in the entire data distribution), it is important to look at the second-order derivative fluctuations to visualise such latent or unobvious features. Although the second-order differential value fluctuates significantly, the trend in the fluctuation can be obtained by a three-point running approximating the secondary derivative. As a result, we found that the boundary of each facies type of the seafloor corresponds to the folding point in the trend of the second-order differential values of the histogram, as described below.

In the MR15-02south data, the geographical distribution of the seafloor showing 5.8 dB (blue contour line in Figure 2) almost corresponds with the facies boundary between Type-L and Type-M. The tendency of the first- and second-

order differential values changes drastically at an intensity of 5.8 dB (blue vertical line in Figure 3(a)). Specifically, the second-order differential values show two oscillations from positive to negative in the backscatter intensity from 4.0 to 5.8 dB, followed by a gradual decrease in the backscatter intensity between 5.8 and 6.4 dB. Such changes in the trend of the second-order differential values reflect changes in the histogram shape, which then likely indicates a seafloor facies shift from sparse (or barren pelagic sediment) to denser nodule distributions. Therefore, we define the L–M boundary (Table 1) as a backscatter intensity that corresponds to the folding point in the trend of the second-order differential values, indicating an increase in the distribution density of nodules. Moreover, 6.4 dB which approximately geographically corresponds to the boundary between Type-M and Type-H facies (green contour line in Figure 2) is another folding point in the trend of the second-order differential values (green vertical line in Figure 3(a)). In this case, changes in the trend of the second-order differential value show that there is a change in the gradient of the three-point running mean for the secondary derivative (orange line in Figure 3). Since the trend of the second-order differential value reflects the essential histogram shape of the original backscatter intensity data, the folding points described above probably indicate changes in nodule distribution features. Therefore, we define the M–H boundary (Table 1) where the backscatter intensity corresponds with the folding point in the trend of the second-order differential values, indicating a further increase in the distribution density of nodules and appearance of large nodules. With an increase in intensity in the domain above 7.45 dB (black vertical line in Figure 3(a)), we recognise a smooth increase in the first- and second-order differential values. The region of Type-V facies corresponds well to the region showing an intensity of more than 7.45 dB (black contour line in Figure 2). Therefore, we define the H–V boundary (Table 1) as a backscatter intensity corresponding to the folding point of the trend in the first- and second-order differential values, indicating a dense distribution of large nodules.

These observations demonstrate that we can determine changes in the geological features based on the histogram of backscatter intensity from the seafloor. Identification of the actual intensity value for geological boundary from several folding points of the trend in the first- and second-order differential values must be based on geographical correspondence between the intensity value and observed
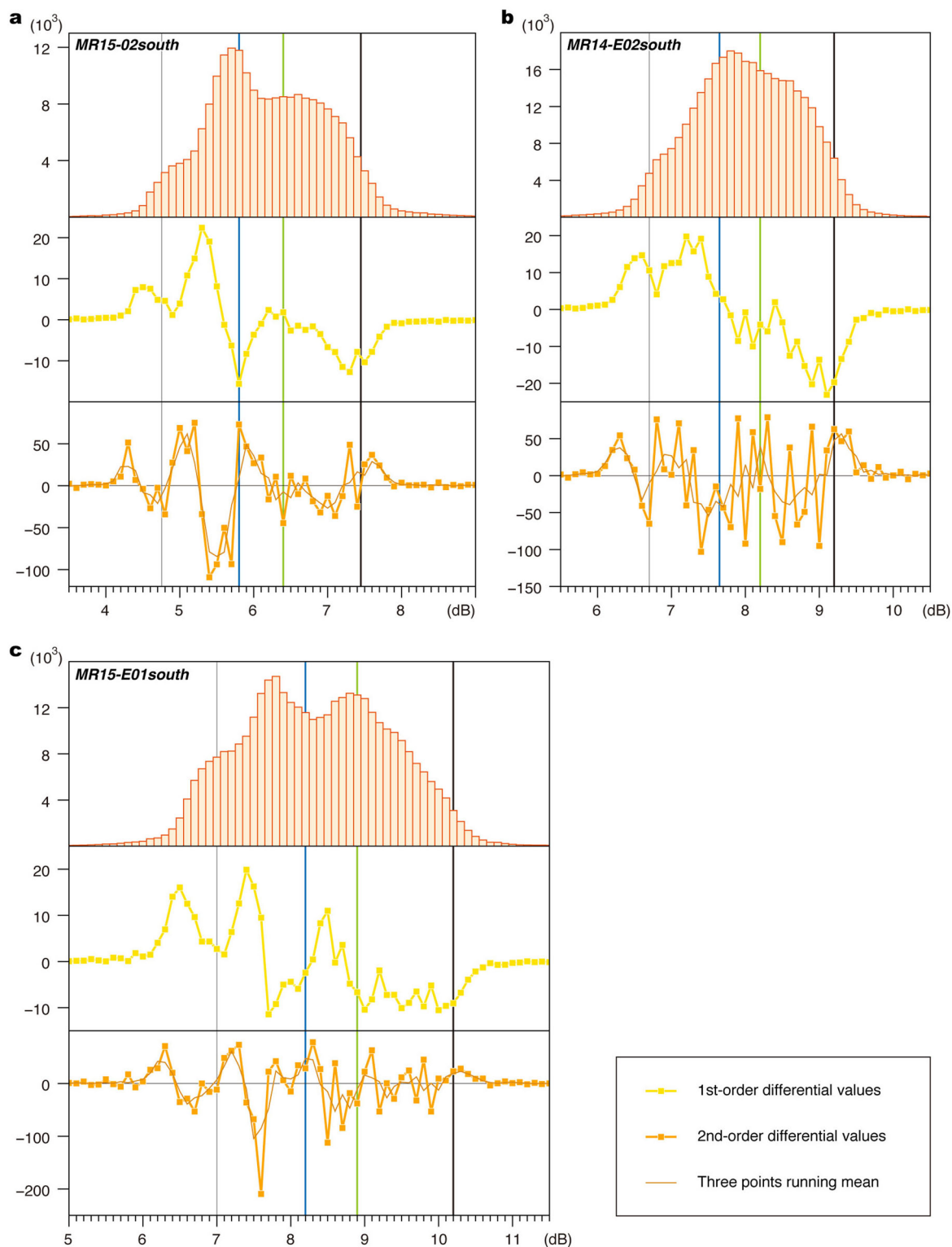
Figure 3. Histogram of backscatter intensity and diagrams of the first- and second-order differential values for the type location. Histogram and diagrams for multiple sets of backscatter intensity data (**a,** MR15-02south; **b,** MR14-E02south; **c,** MR15-E01south) are based on the data of the type location shown in the map of Figure 2. Values for the boundary intensities between different types of seafloor facies (L–M, M–H and H–V boundaries; see the main text, Figure 2 and Table 1 for details) are indicated by blue, green and black vertical lines, respectively. The grey vertical line indicates the value of the base intensity (see main text and Table 1 for details).

geological boundary, as considered using Figures 2 and 3. For this study, we determined the presence of a change from barren pelagic sediment to a ferromanganese nodule field or systematic variations in the nodule density distribution and average nodule diameter. We note that regions with the high backscatter intensities are also regions with ferromanganese crust, as described in the previous section. Even though actual changes in the facies are gradual, especially for the nodule distributions, a particular value defines each boundary intensity, shown as a single line on the map.

This is due to the fact that the spatial scale of change in the facies is lower than the gridding interval of the backscatter intensity data.

For the two other datasets (MR14-E02south and MR15-E01south) in the same type location, the shapes of the histograms and the first- and second-order differential values (Figure 3(b,c)) are different from those of the MR15-02south data (Figure 3(a)). These differences can be attributed to the differences in data frequency due to the different MBES observation tracks during each cruise. As mentioned in Section 3, data variance of each data set for this region fully covers the entire data variance of each data sets. Therefore, data bias also should be limited as the case of MR15-02south data. To identify the boundary intensity between the different seafloor facies, we found two common and fundamental features in the histograms for the three datasets. One is the negative peak of the second-order differential values in the domain of lowest intensity. Thus, we define "the base intensity" (grey vertical lines in Figure 3) as an intensity that gives the inflection point at the higher-intensity-side of the peak (i.e. an intensity at which the second-order differential value almost equals to zero) on the lowest intensity portion of the histogram. The base intensities for the MR15-02south, MR14-E02south and MR15-E01south data are 4.75, 6.70 and 7.00 dB, respectively (Figure 3; Table 1). We confirmed that the geographical distributions of the seafloor showing the base intensity are similar for all datasets (white contour line in Figure 2). The second common feature characterising the domain of intensity higher than that of the H–V boundary of the histogram is a smooth increase in the first- and second-order differential values with increasing intensity. The H–V boundaries for the MR15-02south, MR14-E02south, and MR15-E01south data are 7.45, 9.20, and 10.20 dB, respectively (Figure 3; Table 1).

Based on the constraint that the L–M and M–H boundaries should be the folding point on the overall trend of the second-order differential values between the base intensity and the H–V boundary, we defined L–M boundaries of 7.65 and 8.20 dB and M–H boundaries of 8.20 and 8.90 dB for the MR14-E02south and MR15-E01south data, respectively (Figure 3; Table 1). The changes in gradient for the secondary derivative, which are approximated using a three-point running mean (orange line in Figure 3), allow us to define the folding point along the trend of the second-order differential values. Identification of the geological meaning of the different values of the L–M and M–H boundaries of each dataset is verified by mapping these boundary values (Figure 2). Furthermore, Figure 3 demonstrates the important fact that the base and boundary intensities appear at similar intervals on the histogram, from lower to higher intensity. To obtain quantitative observation, we define and calculate the relative interval (RI) of each boundary value (Table 1). MH_{RI} is calculated using the following equation:

$$MH_{RI} = {(i_M - i_B)} / {(i_H - i_B)} \qquad (1)$$

where i_M is the intensity value of the L–M boundary, i_H is the intensity value of the M–H boundary and i_B is the base intensity. HV_{RI} is calculated using the following equation:

$$HV_{RI} = {(i_H - i_B)} / {(i_V - i_B)} \qquad (2)$$

where i_V is the intensity value of the H–V boundary. The calculated MH_{RI} and HV_{RI} values of each dataset are very similar (Table 1), which indicates that our definitions of each boundary accurately extract the inherent geometric features in each intensity data histogram. Overall, we consider that the folding points in the trend of the second-order differential values mirror the boundary intensities for the different seafloor facies, even if the absolute intensity values are different in each dataset. Conclusively, important constraints for identification of intensity values (or the folding points in the trend of the second-order differential values of the histogram) indicating the same geologic boundaries for the different datasets are coherence of geographical distribution and similarity of the RI value of each boundary intensity.

4.2. Verification of histogram analysis

The three datasets discussed above were obtained using the same vessel-equipped MBES. As a next step, we aimed to verify whether the histogram analysis of backscatter intensity is a robust approach for data collected using the different MBESs across different regions and during different observation periods. We therefore re-interpret previous data (Machida et al. 2016) collected during the cruise YK10-05 of *R/V Yokosuka* (YK10-05SiteA and YK10-05SiteB). The representative area was selected from the YK10-05SiteB data (Figure 4), which covered the variance in the backscatter data and included ground-truth observations using the *SHINKAI 6500* (dive Nos. 6K#1459 and 6K#1501). The histogram appears as a broad single peak in the frequency distribution. In the such case, intrinsic changes in frequency should be visualised by the second-order derivative fluctuations. Based on the same identification criteria for data collected by *R/V Mirai*, we identified the base intensity at 4.8 dB and folding points in the trend of the second-order differential values at 9.20, 11.80 and 16.40 dB (Figure 4; Table 1). Verification of ground-truthing observations during the 6K#1459 and 6K#1501 dives (Figure 4) revealed that the identified folding points in the trend of the second-order differential values for the YK10-05SiteB data indicate the same geological boundaries as the case investigated by *R/V Mirai*, as described in the following. Seafloor showing a backscatter intensity less than 9.20 dB (6K#1459 stop 6 and 6K#1501 stop 1; Figures 4, S8 and S9, supplementary material) is composed of a sparse (or no) distribution of small nodules; that is, the Type-L facies. The distribution density of nodules gradually increases with increasing backscatter intensity along the dive track between stops 4 and 6 of 6K#1459 and between stops 1 and 2 of 6K#1501 (Figures 4, S8 and S9, supplementary material). These observations indicate that the facies of the seafloor changes from Type-L to Type-M at an intensity of 9.20 dB, which identifies the L–M boundary in the case of the YK10-05SiteB data. We also confirmed that 11.80 and 16.40 dB correspond to the M–H and H–V boundaries, respectively, on the basis of
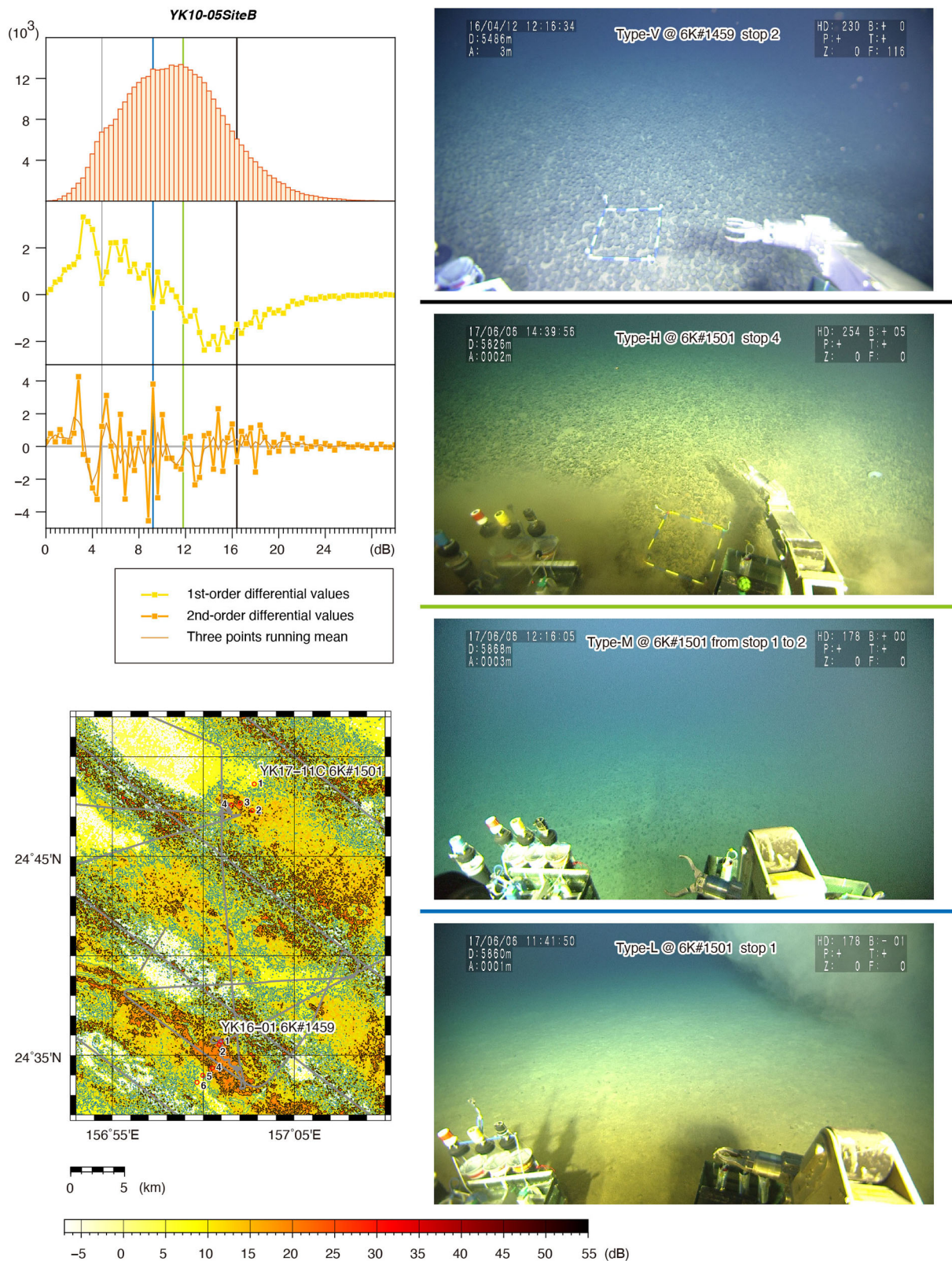
Figure 4. Histogram, diagrams and map of backscatter intensity, together with photographs for ground-truthing to verify our analysis. The presented backscatter intensity data (YK10-05SiteB) were previously obtained during the cruise YK10-05 of *R/V Yokosuka* (Machida et al. 2016). The range of the map is indicated by a white box in Figure S5 (supplementary material). Grey lines illustrate ship track of each cruises. Photographs in the right half show the types of seafloor facies (Type-L, Type-M, Type-H and Type-V facies; see the main text for details) and are taken at stops (red circles in map, with numeric annotation indicating stop numbers) during two dives of the submersible *SHINKAI 6500* (dive Nos. 6 K#1459 and #1501; see supplementary material for details). One side of the blue/yellow-banded box is 50 cm. The first- and second-order differential values are calculated from the frequency of histograms for the YK10-05SiteB data and are shown as a histogram. The blue, green and black lines indicate values for the boundary intensities between the different types of seafloor facies, i.e. the L–M, M–H and H–V boundaries (see the main text for details; Table 1), respectively. Geographic distributions of the seafloor showing the values of the boundary intensities are illustrated as same-Coloured contour lines in the intensity maps. The grey vertical line in the histogram indicates the value of the base intensity (see main text and Table 1 for details). The white contour line in the map illustrates geographic distribution of the seafloor, showing the base intensity.

observations at 6 K#1459 stop 4 and 6 K#1501 stop 4 (Type-H facies) and at 6 K#1459 stops 1 and 2 (Type-V facies) (Figures 4, S8 and S9, supplementary material). On the seafloor showing Type-H and Type-V facies, we recognised that the maximum diameter of spherical nodules is approximately 10 cm, as reported previously by Machida et al. (2016); this is comparable with the area investigated by R/V Mirai. Furthermore, the RI of the boundary intensities (i.e. MH$_{RI}$ and HV$_{RI}$) for the data collected by R/V Yokosuka are almost identical to those collected by R/V Mirai (Table 1). These lines of evidence indicate that the underlying features in the histogram of backscatter intensity and their correspondence with geological characteristics on the seafloor are robust, regardless of technical differences in the MBESs.

4.3. Influence of topography and stratigraphy to backscatter intensity

Figure 5 shows the correlations between topography gradient and backscatter intensity for both representative areas for the MR15-02south and YK10-05SiteB datasets. We are unable to recognise any systematic correlations between gradient distribution and backscatter intensity or any blurriness in the backscatter data owing to the topography, particularly in the regions which have a slope gradient of less than 10 degrees. Moreover, horizontal or vertical data variance on the scatter diagrams based on data from the representative areas (Figure 5) together with the data of the entire dataset, suggest that no correlations exist between topography and backscatter intensity. We further conducted an identical correlation evaluation using regional scatter diagrams of all dive sites (Figures S7–S28). These diagrams verify that correlations are poor at any spatial scale, except for the region where nodule density increases on the mound, such as stops from 1 to 4 of the 6 K#1459 dive (Figures S7 and S8, supplementary material) or stops 3 and 4 of the 6 K#1465 dive (Figures S12 and S13, supplementary material). Therefore, these results indicate that undulating topography does not affect the strength of the backscatter intensity at least in areas whose topographic gradient is lower than 10 degrees.

Recent acoustic surveys, using a sub-bottom profiler (Nakamura et al. 2016), have shown the stratigraphic features in the southern half of the Japanese EEZ around the Minamitorishima Island, which includes all dive sites in this study except for 6 K#1466 and 6 K#1503 dives, can be classified into as the T$_I$ echo type. T$_I$-type sediment thickness is several tens of metres and does not vary regionally, indicating that sediment thickness does not control variations in backscatter intensity. Acoustically opaque regions (O-type facies; Nakamura et al. 2016) correspond to hard rock outcrops covered by ferromanganese crust (sites 6 K#1463, 6 K#1497 and 6 K#1499; Figures S14, S15, S21, S22, S25 and S26, supplementary material) and the regions with lava that intrudes into the pelagic sediment (site 6 K#1466; Figures S19 and S20, supplementary material) are both characterised by high backscatter intensity. Moreover, the stratigraphic features in the northern part of the Japanese EEZ are commonly classified as L echo type. L-type sediment is composed of thick barren pelagic sediments (Nakamura et al.

2016) and is regionally distributed where there is lower backscatter intensity than at the L–M boundary, as shown by the MR14-E02transit, MR15-E01north and MR15-02transit datasets (Figures S3, S5 and S29–S31, supplementary material). As described previously, we observed a lack of ferromanganese nodules in the L-type sediment at site 6 K#1503 (Figures S27 and S28, supplementary material). This result suggests that we actually observed only a change in backscatter intensity, which represents a change in the features on or variation in seafloor surface hardness.

4.4. Data integration

As there is no influence from topography (slope gradient) and stratigraphy (sediment thickness), ground-truth relations between backscatter intensity and geological features are applicable to other regions. Furthermore, if one identifies the unique boundary intensities each indicating the same geologic boundaries for the other datasets (Figures S29–S32, supplementary material) and/or if the geographical distributions of the identified base and boundary intensities between the different datasets are confirmed (Figures 2 and S33–S35, supplementary material), we can linearly integrate several backscatter intensity datasets (Figure S36; Table S1, supplementary material). The integration should be based on multiple boundary intensities that we identified from the histograms. The constant RI value for the boundary intensities from any dataset's base intensity (Table 1) critically constrains the identification of the boundary intensities from the numerous folding points in the trend of the second-order differential value. In particular, this latter constraint ensures linear fitting of the thresholds used to adjust each dataset to the arbitrary standard data. The standardised intensity (I_{SD}) is calculated from the original intensity (I_{OR}) using the equation

$$I_{SD} = {(I_{OR} - \beta_{OR})}/{\kappa} + \beta_{SD} \tag{3}$$

where κ is a conversion factor, β_{OR} is the base intensity of the original dataset and β_{SD} is the base intensity of the standard dataset. The conversion factor (κ) is calculated using the equation

$$\kappa = {\alpha_{OR}}/{\alpha_{SD}} \tag{4}$$

where α is the slope of the regression line defined by the method of least squares for a two-dimensional matrix of all the identified base and boundary intensities and sequentially numbered integers for the original (OR) or standard (SD) dataset. ASCII-formatted three-dimensional data consisting of longitude, latitude and I_{SD} for all of datasets are integrated into a single data, followed by conversion to a grid file (i.e. integrated data) using the "xyz2grd" command of the GMT software (Wessel and Smith 1998). In this study, all datasets were linearly fitted to the MR15-02south data, which was used as a standard, on the basis of their thresholds. Our identification of the thresholds is shown in Figures 3, 4, and S29–S32 (supplementary material) and Table 1. The consistency on the thresholds for each dataset was considered by their mapping in the representative region overlapping two (or more) datasets (Figures 2 and
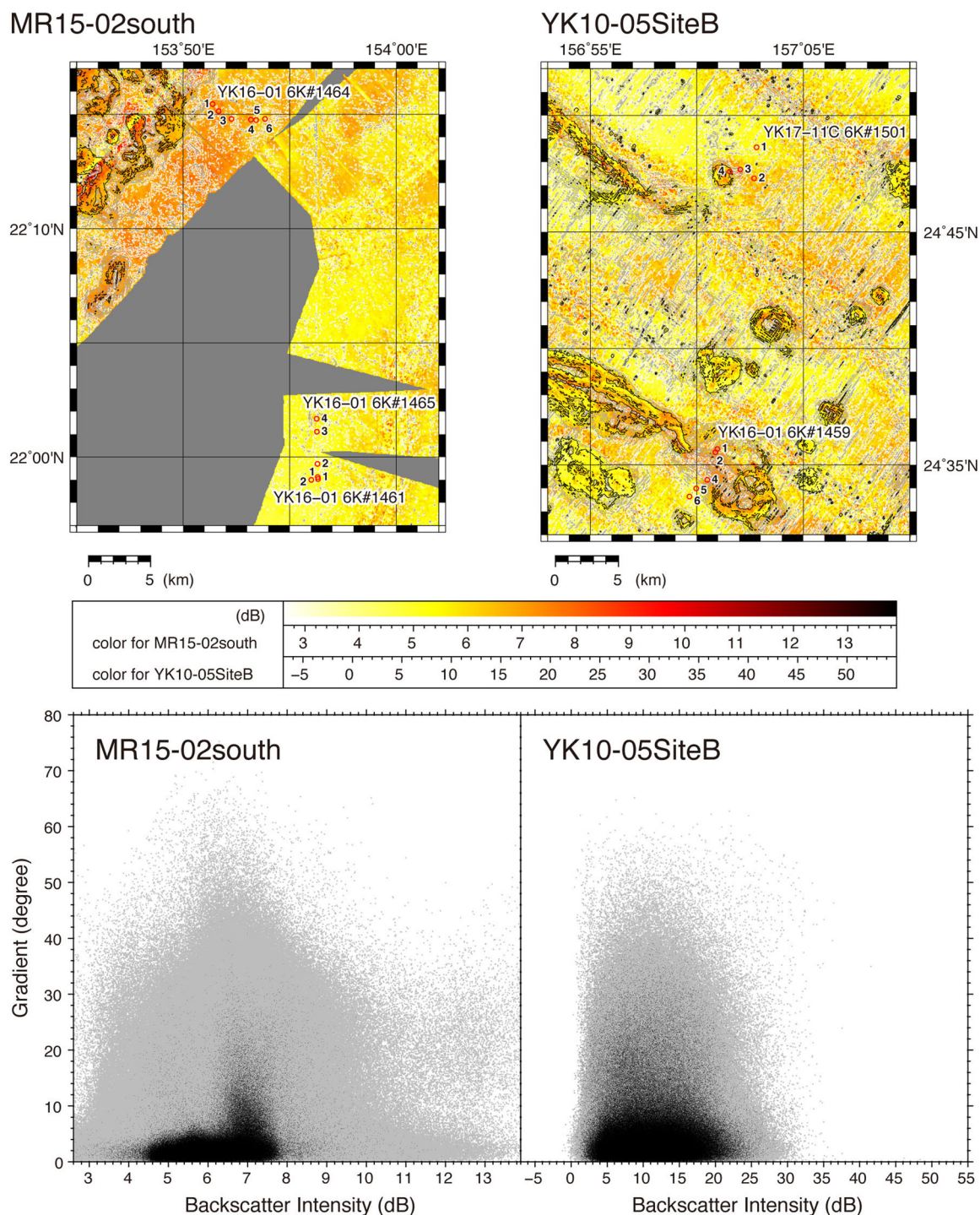
Figure 5. Map and scatter plot showing the correlation between backscatter intensity and the topography gradient in the type location for the MR15-02south and YK10-05SiteB data sets. The range of the map for each type location is identical to Figures 1 and 4. The white and grey contour lines indicate gradient values of 3 and 5, respectively, and the black contour lines indicate gradient values 10 and 30 degrees. The grey and black dots indicate the entire data set and data from the type locations, respectively.

S33–S35) and results of ground-truthing observations by the submersible *SHINKAI 6500* (Figures S7–S28 and Table S1, supplementary material).

4.5. Deriving a simple scheme for reconnaissance exploration

Based on our results, we finally propose a simple reconnaissance exploration method for deep-sea ferromanganese deposits using

a vessel-equipped MBES. Initially, to cover a wide range of backscatter intensities, various terrains from the deep seafloor to the seamount should be investigated. This is required because soft sediments are expected to be deposited on the deep seafloor and these show low intensity in the cases where nodules are absent; this contrasts with the situation for seamounts, which commonly show higher intensity due to a lack of sediment deposition and thus an exposure of hard materials (e.g. seamount basalts with a ferromanganese crust). As previously described, our observations
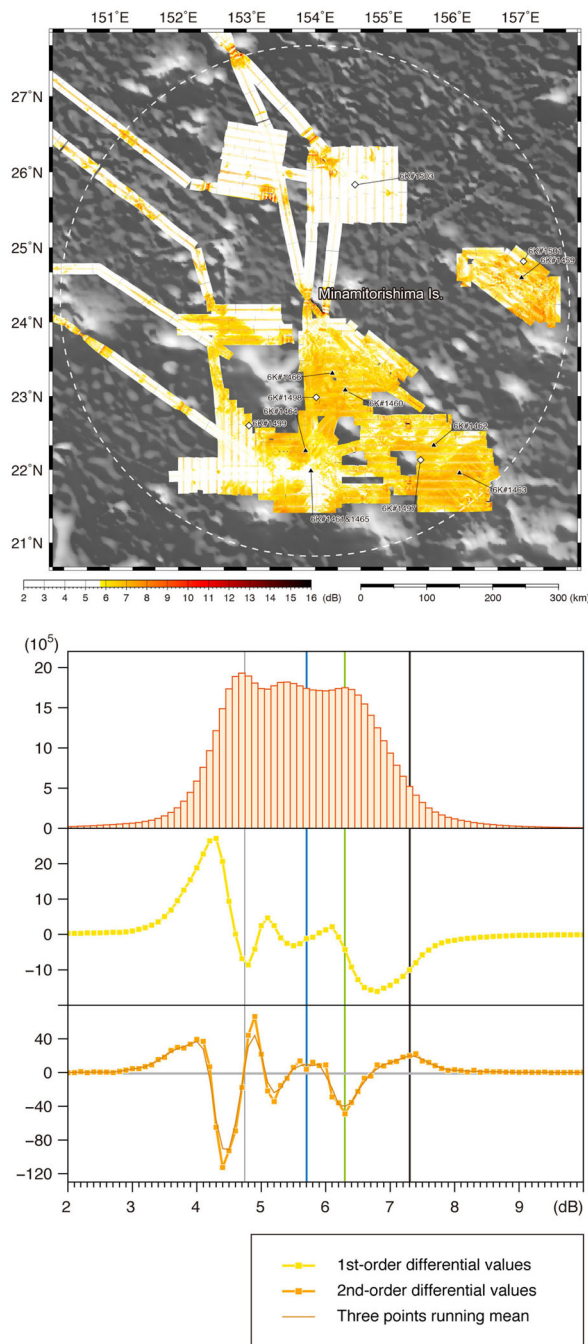
Figure 6. Integrated backscatter intensity map showing the broad distribution of ferromanganese nodules and crusts in the Japanese EEZ around Minamitorishima Island. Backscatter intensity data are established by the integration of nine datasets (MR14-E02south, MR15-E01south, MR15-E01north, MR15-02south, MR14-E02transit, MR15-E01transit, MR15-02transit and YK10-05SiteA and B) on the basis of the boundary intensities between the different types of seafloor facies (see the materials and methods section for details). The first- and second-order differential values are calculated from the frequency of histograms for the integrated data and are shown as a histogram. The blue, green and black vertical lines in the histogram and diagrams indicate values for the boundary intensities between different types of seafloor facies, i.e. the L–M, M–H and H–V boundaries (see the main text for details; Table 1), respectively. A grey vertical line in the histogram and diagrams indicates the value of the base intensity (see the main text for details; Table 1). Regions showing backscatter intensities lower than those observed for the L–M boundary (5.72 dB) are Coloured white on the map to clearly show the broad distribution of higher intensity, which indicates the distribution of ferromanganese nodules and crusts. Uncropped integrated intensity data are shown in Figure S1. Black symbols with numeric annotation indicate observation sites using the submersible SHINKAI 6500. The range of the map is same as that considered in Figure 1.

using SHINKAI 6500 clarified that the field of nodules continuously connects to outcrops of crust (Figures S14, S15, S21, S22, S25 and S26, supplementary material). Recent study (Azami et al. 2018) shows that other seamounts in our survey area are also commonly covered by ferromanganese crusts. Therefore, we believe that the slope of a seamount showing a higher backscatter intensity should be included in our target area. Topographic data estimated from satellite gravity measurements, although being of lower spatial resolution than that of MBES, can help to plan effective survey lines during investigations. As a next step, a histogram of the gridded intensity data should be produced and used to calculate the first- and second-order differential values and identify their folding points. Subsequently, we should only observe the lowest intensity region so as to guarantee that ground-truthing using a submersible (or a box corer and/or deep-sea camera for added simplicity) can be undertaken. If we observe an absence (or small number) of nodules in the lowest intensity region, exploration should be focussed only on regions showing higher intensity than the folding point (i.e. the boundary intensity) in the trend of the second-order differential values of the histogram.

By identifying the boundary intensity(ies) as the threshold(s) indicating a meaningful geologic boundary, we can integrate several backscatter datasets to form a single dataset and immediately estimate the dimensions of geological facies using the "grdvolume" command of the GMT software (Wessel and Smith 1998). Therefore, this new reconnaissance exploring protocol enables us to quantitatively estimate the geographical distribution of resources across a wide area on the deep-sea floor in a relatively simple and cost-effective manner. In the case of this study (Figures 6 and S36, supplementary material), we integrated nine datasets to map the backscatter intensity of a region of approximately 155,500 km^2 in the Japanese EEZ around Minamitorishima Island. Based on the intensity value of the L–M boundary identified using the histogram of the integrated dataset (Figure 6; Table 1) and the regions where there is a slope gradient of less than 10 degrees, it was estimated that the area of the field densely covered by ferromanganese nodules is approximately 61,200 km^2, or approximately 39% of the mapped area. Our visualisation demonstrates that the fields of dense nodules are commonly distributed around seamounts or guyots. Nodules almost fully cover the ocean basin enclosed by several seamounts and guyots, especially in the south-eastern part of the EEZ. Identification of the threshold of the backscatter intensity corresponding to the transition of different geological facies is the key to area estimation. We should therefore pay most attention to the change in the overall trend of second-order differential values in the histogram of backscatter intensity. It also should be noted that when histograms are produced using a whole dataset, information on the minor geology is not always easily identified. In that case, it is important to narrow down the target of the data analysis, from the whole investigated region to a limited area covering the entire variance of the data.

The detection of hard materials based on acoustic reflection is the fundamental principle of our simple reconnaissance

exploration method. As an example of application of this method for the other kind of solid mineral resources, if we consider the regions having a slope gradient of more than 10 degrees for our data presented in this study, we can estimate the total area of the field for the ferromanganese deposit (nodules and even crusts in some cases), i.e., approximately $70,500 \, km^2$, or approximately 45% of the mapped area. Further, the detailed correlation between the backscatter intensity data and the features of crust or sulphide distribution should be investigated in a future study. Scrutiny, for example detailed mapping using autonomous underwater vehicles (AUV), can be carried out efficiently if it is done after narrowing down the exploration area using our protocol. The basic concept of our method, histogram analysis for the classification of seafloor facies and data integration, should be applicable to multibeam backscatter data obtained using other equipment including side scan sonar equipped on AUV. Therefore, all types of solid mineral resources, such as the hydrothermal sulphide deposits and ferromanganese crusts as well as nodules, and any backscatter data from the other waters not only in the NW Pacific should be considered for the future application and development of our method.

5. Conclusions

Our ground-truthing observations obtained using the submersible *SHINKAI 6500* revealed a correlation between the backscatter intensity and the seafloor facies on the nodule distributions, thereby confirming the integration of multiple datasets to provide visualisation and quantitative estimations with respect to the distribution of ferromanganese deposits over an area spanning thousands of square kilometres. The data integration theory presented in this study states that majority of the existing MBES data can be calibrated to an arbitrary backscatter intensity scale when each data set contains an overlapping region. Further, the requirement of unspecific data collection, data processing, and histogram analysis, and of limited ground truth observations are also advantages with respect to expeditious and exhaustive reconnaissance exploration. Therefore, our method can contribute to the future mining of deep-sea mineral resources by effectively and efficiently exploring the abyssal floor that has incapacitated an extensive survey by electromagnetic wave since the last century.

Acknowledgements

Disclosure statement

No potential conflict of interest was reported by the author(s)

Funding

References

Azami, K., N. Hirano, S. Machida, K. Yasukawa, and Y. Kato. 2018. Rare Earth Elements and Yttrium (REY) Variability with Water Depth in Hydrogenetic Ferromanganese Crusts. *Chemical Geology* 493: 224–233. doi:10.1016/j.chemgeo.2018.05.045.

Chadwick, W. W., Jr., S. G. Merle, N. J. Buck, J. W. Lavelle, J. A. Resing, and V. Ferrini. 2014. Imaging of CO_2 Bubble Plumes above an Erupting Submarine Volcano, NW Rota-1, Mariana Arc. *Geochemistry, Geophysics, Geosystems* 15 (11): 4325–4342. doi:10.1002/2014GC005543.

Chakraborty, B., and V. Kodagali. 2004. Characterizing Indian Ocean Manganese Nodule-Bearing Seafloor Using Multi-Beam Angular Backscatter. *Geo-Marine Letters* 24 (1): 8–13. doi:10.1007/s00367-003-0153-y.

Chunhui, T., J. Xiaobing, B. Aifei, L. Hongxing, D. Xianming, Z. Jianping, G. Chunhua, W. Tao, and R. Wilkens. 2015. Estimation of Manganese Nodule Coverage Using Multi-Beam Amplitude Data. *Marine Georesources & Geotechnology* 33: 283–288. doi:10.1080/1064119X.2013.806973.

Cochonat, P., R. Le Suavé, C. Charles, B. Greger, M. Hoffert, J. P. Lenoble, J. Meunier, and G. Pautot. 1992. First in Situ Studies of Nodule Distribution and Geotechnical Measurements of Associated Deep-Sea Clay (Northeastern Pacific Ocean). *Marine Geology* 103 (1–3): 373–380. doi:10.1016/0025-3227(92)90027-F.

Craig, J. D. 1979. The Relationship Between Bathymetry and Ferromanganese Deposits in the North Equatorial Pacific. *Marine Geology* 29 (1-4): 165–186. doi:10.1016/0025-3227(79)90107-5.

de Moustier, C. 1985. Inference of Manganese Nodule Coverage from Sea Beam Acoustic Backscattering Data. *Geophysics* 50 (6): 989–1001. doi:10.1190/1.1441976.

de Moustier, C. 1986. Beyond Bathymetery: Mapping Acoustic Backscattering from the Deep Seafloor with Sea Beam. *The Journal of the Acoustical Society of America* 79 (2): 316–331. doi:10.1121/1.393570.

de Moustier, C., and H. Matsumoto. 1993. Seafloor Acoustic Remote Sensing with Multibeam Echo-Sounders and Bathymetric Sidescan Sonar Systems. *Marine Geophysical Researches* 15 (1): 27–42. doi:10.1007/BF01204150.

Hannington, M., J. Jamieson, T. Monecke, S. Petersen, and S. Beaulieu. 2011. The Abundance of Seafloor Massive Sulfide Deposits. *Geology* 39 (12): 1155–1158. doi:10.1130/G32468.1.

Hein, J. R., K. Mizell, A. Koschinsky, and T. A. Conrad. 2013. Deep-Ocean Mineral Deposits as a Source of Critical Metals for High- and Green-Technology Applications: Comparison with Land-Based Resources. *Ore Geology Reviews* 51: 1–14. doi:10.1016/j.oregeorev.2012.12.001.

Hirano, N., E. Takahashi, J. Yamamoto, N. Abe, S. P. Ingle, I. Kaneoka, T. Hirata., et al. 2006. Volcanism in Response to Plate Flexure. *Science* 313 (5792): 1426–1428. doi:10.1126/science.1128235.

Hirano, N., A. A. P. Koppers, A. Takahashi, T. Fujiwara, and M. Nakanishi. 2008. Seamounts, Knolls and Petit Spot Monogenetic Volcanoes on the Subducting Pacific Plate. *Basin Research* 20 (4): 543–553. doi:10.1111/j.1365-2117.2008.00363.x.

Hirano, N., S. Machida, N. Abe, T. Morishita, A. Tamura, and S. Arai. 2013. Petit-Spot Lava Fields off the Central Chile Trench Induced by Plate Flexure. *Geochemical Journal* 47 (2): 249–257. doi:10.2343/geochemj.2.0227.

Hirano, N., M. Nakanishi, N. Abe, and S. Machida. 2016. Submarine Lava Fields in French Polynesia. *Marine Geology* 373: 39–48. doi:10.1016/j.margeo.2016.01.002.

International Hydrographic Organization 2008. IHO Standards for Hydrographic Surveys, 5th ed. International Hydrographic Organization Special Publication S-44, 28pp. http://hdl.handle.net/11329/388.

Kasaya, T., H. Machiyama, K. Kitada, and K. Nakamura. 2015. Trial Exploration for Hydrothermal Activity Using Acoustic Measurements at the North Iheya Knoll. *Geochemical Journal* 49 (6): 597–602. doi:10.2343/geochemj.2.0389.

Kato, Y., K. Fujinaga, K. Nakamura, Y. Takaya, K. Kitamura, J. Ohta, R. Toda, T. Nakashima, and H. Iwamori. 2011. Deep-Sea Mud in the Pacific Ocean as a Potential Resource for Rare-Earth Elements. *Nature Geoscience* 4 (8): 535–539. doi:10.1038/ngeo1185.

Lee, S. H., and K.-H. Kim. 2004. Side-Scan Sonar Characteristics and Manganese Nodule Abundance in the Clarion—Clipperton Fracture Zones, NE Equatorial Pacific. *Marine Georesources & Geotechnology* 22: 103–114.

Ma, Y., A. H. Magnuson, V. K. Varadan, and V. V. Varadan. 1986. Acoustic Response of Manganese Nodule Deposits. *Geophysics* 51 (3): 689–698.

Machida, S., K. Fujinaga, T. Ishii, K. Nakamura, N. Hirano, and Y. Kato. 2016. Geology and Geochemistry of Ferromanganese Nodules in the Japanese Exclusive Economic Zone around Minamitorishima Island. *Geochemical Journal* 50 (6): 539–555.

Mitchell, N. C. 1993. A Model for Attenuation of Backscatter Due to Sediment Accumulations and Its Application to Determine Sediment Thicknesses with GLORIA Sidescan Sonar. *Journal of Geophysical Research: Solid Earth* 98 (B12): 22477–22493. doi:10.1029/93JB02217.

Nakamura, K., S. Kawagucci, K. Kitada, H. Kumagai, K. Takai, and K. Okino. 2015. Water Column Imaging with Multibeam Echo-Sounding in the mid-Okinawa Trough: Implications for Distribution of Deep-Sea Hydrothermal Vent Sites and the Cause of Acoustic Water Column Anomaly. *Geochemical Journal* 49 (6): 579–596.

Nakamura, K., S. Machida, K. Okino, Y. Masaki, K. Iijima, K. Suzuki, and Y. Kato. 2016. Acoustic Characterization of Pelagic Sediments Using Sub-Bottom Profiler Data: Implications for the Distribution of REY-Rich Mud in the Minamitorishima EEZ, Western Pacific. *Geochemical Journal* 50 (6): 605–619. doi:10.2343/geochemj.2.0433.

Oikawa, M., N. Watanabe, T. Hashimoto, T. Yoshida, and S. Chiba. 2010. The Uncertainties and the Data Management of Deep Water Bathymetric Data Obtained with Multibeam Echo Sounders. *Report of Hydrographic and Oceanographic Researches* 46: 39–46. in Japanese with English abstract)

Piper, D. Z., and J. R. Blueford. 1982. Distribution, Mineralogy, and Texture of Manganese Nodules and Their Relation to Sedimentation at DOMES Site a in the Equatorial North Pacific. *Deep Sea Research* 29 (8): 927–952.

Roman, C., G. Inglis, J. I. Vaughn, C. Smart, B. Douillard, and S. Williams. 2012. The development of high-resolution seafloor mapping techniques. In Bell, K.L.C., Elliot, K., Martinez, C., Fuller, S. A. (eds.), *New Frontiers in Ocean Exploration: The E/V Nautilus and NOAA Ship Okeanos Explorer 2011 Field Season. Oceanography*, 25 (supplement): 42–45.

Sharma, R., and V. N. Kodagali. 1993. Influence of Seabed Topography on the Distribution of Manganese Nodules and Associated Features in the Central Indian Basin: A Study Based on Photographic Observations. *Marine Geology* 110 (1/2): 153–162. doi:10.1016/0025-3227(93)90111-8.

Sharma, R., N. H. Khadge, and S. Jai Sankar. 2013. Assessing the Distribution and Abundance of Seabed Minerals from Seafloor Photographic Data in the Central Indian Ocean Basin. *International Journal of Remote Sensing* 34 (5): 1691–1706. doi:10.1080/01431161.2012.725485.

Tolstoy, I. 1983. Acoustic Estimation of Deep Sea Floor Nodule Densities. *Geophysics* 48 (11): 1450–1452. doi:10.1190/1.1441429.

Usui, A., A. Nishimura, M. Tanahashi, and S. Terashima. 1987. Local Variability of Manganese Nodule Facies on Small Abyssal Hills of the Central Pacific Basin. *Marine Geology* 74 (3-4): 237–275. doi:10.1016/0025-3227(87)90053-3.

Valsangkar, A. B., and J. M. S. Rebello. 2015. Significance of Size in Occurrence, Distribution, Morphological Characteristics, Abundance, and Resource Evaluation of Polymetallic Nodules. *Marine Georesources & Geotechnology* 33: 135–149. doi:10.1080/1064119X.2013.815673.

Wiedicke, M. H., and M. E. Weber. 1996. Small-Scale Variability of Seafloor Features in the Northern Peru Basin: Results from Acoustic Survey Methods. *Marine Geophysical Researches* 18 (5): 507–526. doi:10.1007/BF00310067.

Wessel, P., and W. H. F. Smith. 1998. New, Improved Version of the Generic Mapping Tools Released. *Eos, Transactions American Geophysical Union* 79 (47): 579. doi:10.1029/98EO00426.